Applied Physics B (2021) 127:140
https://doi.org/10.1007/s00340-021-07689-4

Applied Physics B
Lasers and Optics

In-situ plasma monitoring by optical emission spectroscopy during pulsed laser deposition of doped Lu_2O_3

S. Irimiciuc[1,2] · J. More-Chevalier[2] · S. Chertpalov[2] · L. Fekete[2] · M. Novotný[2] · Š. Havlová[2,3] · M. Poupon[2] · T. Zikmund[2] · K. Kůsová[2] · J. Lančok[2]

Received: 16 March 2021 / Accepted: 6 September 2021 / Published online: 16 September 2021

Abstract
The control and arguably the tailoring aspect of technologies like pulsed laser deposition (PLD) rises from understanding the chemistry hidden by the laser generated plasma. With the continuous transition towards thin films with complex structures and geometries, the comprehension of the fundamental processes during the film deposition becomes critical. During the PLD of Mo and Eu-doped Lu_2O_3, optical emission spectroscopy was implemented for in-situ plasma monitoring. The spatial distribution of individual elements revealed the structuring of a stoichiometric plasma while the formation of LuO molecule within the plasma plume is seen as being induced by the addition of a minimum 1 Pa of O_2. The energy of the ejected particles was controlled through doping and O_2 pressure. The effect of O_2 pressure over the plasma energy revealed a transition from an atomic dominated region towards a molecular dominated one. The properties of the resulted films were analyzed by XRD, AFM, and photoluminescence techniques and show a strong correlation between the dynamical regime of the plasma and their structural properties.

1 Introduction

Plasma monitoring for real-time control of the pulsed laser deposition (PLD) process has been the key for understanding the complex phenomena of the deposition process. Plasma acts like a medium which transports the material from the target and allows the proper conditions for intricate chemistry that encompasses the main characteristic of PLD: multi-variable tailoring of the thin film properties [1]. There is a wide range of reports on diagnostic tools for laser produced plasmas (LPP) that highlight: mass spectrometry [2], optical emission spectroscopy (OES) [3], laser induced absorption/fluorescence [4], or Langmuir probe [5]. Out of all the monitoring techniques, OES is one of the most desirable as it can offer great flexibility given by the geometry of the optical arrangement [6] and real-time response that could potentially create a feedback loop for controlling PLD process. The main advantages of OES are the non-invasive properties of the technique that can offer both quantitative and qualitative information about the deposition process without directly affecting the technological process. OES was also used to highlight laser produced plasma multi-structuring during expansion [7–9] and different dynamics of plasma components based on particle mass [10], individual melting point, ionization degree [11], etc. Although historically this technique was established for steady plasma discharges with a relatively simple composition (single element plasmas), an adapted approach of this investigation technique, suitable for LPP and its transient nature, is the space- and time-resolved OES [12]. The flexibility of the technique is the main argument to implement OES for real-time monitoring of PLD deposition of complex films.

Several papers touch on this aspect with the group of Th. Lippert reporting on both plasma flip-over and plasma rebound in various conditions of complex multi-element plasmas [13], also showcased, using space time-resolved OES the volume distribution of light and heavy elements during the deposition of $LuMnO_3$ [14] while years before these reports the group of D. Geohegan [15] reported on the formation of complex carbon structures during PLD and plasma stopping during the deposition of CN_x which does

✉ S. Irimiciuc
stefan.irimiciuc@inflpr.ro

1 National Institute for Laser, Plasma and Radiation Physics – NILPRP, 409 Atomistilor Street, Bucharest, Romania

2 Institute of Physics of the Czech Academy of Sciences, Na Slovance 2, Prague, Czech Republic

3 University of Chemistry and Technology, Technicka 5, Prague, Czech Republic

not influence the production of complex thin films. The common thread of these reports is the presence of complex films. Understanding the dynamics of multiple elements and the plasma chemistry of such systems is not an easy task, especially with the rising interest in creating doped thin films, where even the addition of a small concentration of a different material can drastically improve the properties of the final product. The changes in the structure and composition of the doped target will also be reflected by the properties of the laser produced plasmas thus in situ analysis could offer important insight into the deposition process.

Rare-earth (RE) doped Lu_2O_3 as a high-k widegap insulators have been investigated for several applications in microelectronics [16] optoelectronics [17, 18] or scintillators [19]. Different techniques reportedly are used to grow such films, e.g., sol–gel [20], hydrothermal [21] and PLD [16, 22, 23]. Laser ablation of Lu metal in O_2 ambient gas superimposed by a supersonic jet of Ar was reported to create gaseous LuO molecule, where Fourier-Transform microwave spectroscopy was used to determine precisely its molecular constants and structural parameters [24]. PLD provides several possibilities controlling the optical and structural properties of Lu_2O_3:Eu films by varying substrate temperature and oxygen pressure [25]. Recently, PLD was shown to fabricate rocksalt structure LuO with unusual valence of Lu^{2+} previously known as the gaseous phase of Lu_2O_3 [25]. There is a lack of data on the relation of the film properties and plasma at PLD of Lu_2O_3 based materials. This represents the motivation behind our work and is on in-situ characterization of laser produced plasma during PLD process with the aim of correlating the properties of the deposited film with the measurable quantifiable data extracted from the plasma.

In this paper, OES was implemented for implemented for in situ monitoring of the laser induced plasmas for quantitative and qualitative investigations for PLD process during generation of Lu_2O_3 thin films doped with various concentrations of Eu^{3+}. Post-deposition several surface analysis techniques were implemented to characterize the properties of the deposited film. The properties of the film are discussed in the framework of the plasma optical emission spectroscopy study.

2 Materials and methods

2.1 Target manufacturing

The circular targets (1 inch in diameter) of Lu_2O_3:Eu (3 and 5 mol. %) were prepared by mixing of Lu_2O_3 and Eu_2O_3 powders (99,995%, Alchimica s.r.o.) in a mortar, and by pressing the mixture in a pressing die. After that, the targets were sintered in an air atmosphere furnace first at temperature of 1000 °C for 6 – 7 h then at 1200 °C for next 6 – 7 h. To confirm the structure and composition of the targets, we performed XRD, XRF and Raman spectroscopy investigations.

XRD measurements were performed with an Empyrean diffractometer on the ceramic targets to confirmed their structures. The analysis was performed on targets (Fig. 1a). The powder profile was fitted using the JANA2006 software [26] and the fundamental approach method [27] to extract crystallite size parameters. The fundamental approach parameter used were: Primary and secondary radius = 240 mm; receiving slit width 0.055 mm; the fixed divergence Slit angle of 0.5°; source length of 12 mm; sample length of 10 mm; receiving slit length of 14 mm, and primary and secondary soller slit of 2.3° and a radiation profile CuKa5 implement in Jana2006. The structure was refined using a Lu_2O_3 Cif [28] file from ICSD database [29]. One atomic displacement parameter was refined for all atoms.

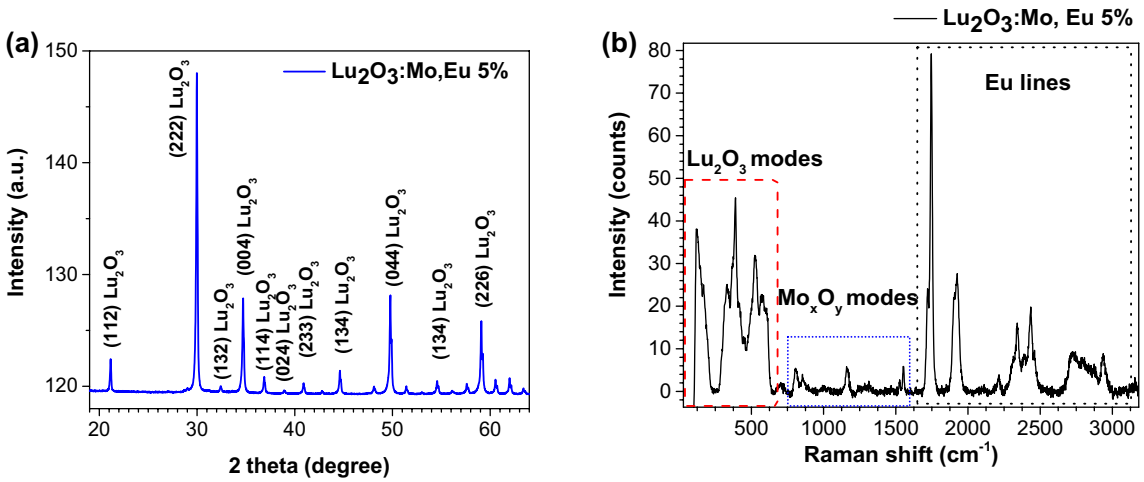

Fig. 1 Diffraction pattern (**a**) and Raman scattering spectra (**b**) from Lu_2O_3: Mo, Eu 5% doped target

Figure 1(b) it is represented the Raman scattering of the Lu_2O_3: Mo, Eu5% doped from the ablated area. Raman scattering spectroscopy carried out at room temperature using a Renishaw InVia Raman spectrometer. Measurements were performed under the following conditions: laser excitation wavelength of 488 nm with laser power of 0.3 mW on the surface of the samples, × 50 Olympus objective, 65 µm slits, and grating of 2400 lines/mm. Lorentz and Gaussian functions were used to fit peaks from the results. The results of the spectra are separated into 3 Raman shift areas: the first one is from 110 cm^{-1} to 620 cm^{-1}, the second comes from 650 cm^{-1} to 1150 cm^{-1}, and the third area comes from 1160 cm^{-1} to 3000 cm^{-1}. Raman peaks detected in the first area are mainly coming from Lu_2O_3 phonon modes and weakly from Eu_2O_3 phonon modes [30]. A low concentration of Mo_xO_y phases with phonon modes corresponding to MoO_2, MoO_3, and Mo_4O_{11}, is detected mainly in the second part of the spectra [31, 32]. Finally, the last spectra part, from 1160 cm^{-1} to 3000 cm^{-1}, shows the line spectra emission of Eu [33].

2.2 Fabrication, structure and surface analyses of films

Fabricated targets were ablated by means of Nd:YAG laser operated at 266 nm wavelength at a repetition rate of 10 Hz leading to a working laser fluence of 5 J/cm^2. The O_2 pressure was varied from high vacuum conditions (1×10^{-4} Pa) up to 5 Pa, while the substrate (fused silica) was placed at 5 cm from the target. The substrate temperature was maintained at 300 K. For growth of each doped Lu_2O_3 films 6000 pulses were used, resulting in films with thicknesses ranging from 120 to 400 nm depending on the O_2 pressure. The thin film thickness was measured using a KLA Tencor P6 profilometer.

The atomic structure and crystalline quality of the films were characterized with the help of X-Ray diffractometer (EMPYREAN, Malvern Panalytical) by grazing incidence (omega = 0.85°) measurements at room temperature. X-ray diffractometer with a Cu line-focus anode source, a parabolic X-ray mirror, and 2-bounce monochromator Ge (220) × 2 producing monochromatic parallel beam (λ(Cu $K_{<\alpha>}$) = 1.540593 Å, U = 45 kV, I = 30 mA) was used. The X-ray diffraction patterns were measured from 2θ = 10° till 2θ = 120° with a step 0.1° and with time per step 5 s.

Atomic force microscopy (AFM Dimension ICON, Bruker) was used to investigate the surface morphology and roughness. The measurements were performed under ambient conditions and images were obtained by the Peak Force Tapping mode using ScanAsystAir tips with scan areas of 1×1 μm^2.

2.3 Optical properties analysis of films

Photoluminescence (PL) spectra were exited using a UV lamp (the 254 nm line, 2 × 6 W) in combination with a 600-nm shortpass filter (Thorlabs). The PL was excited from the face of the sample and the signal was collected at a roughly 45-degree angle with a quartz fiber. Longpass filter (488 nm, Semrock) was used in the collection. The signal was spectrally dispersed by an imaging monochromator (Shamrock 303i, 100 um slit width) using a 300 l/mm grating blazed at 500 nm, coupled with EMCCD camera Newton 971 (cooled to −80 °C, 1600 pixels). The spectra were corrected for the response of the whole collection/detection setup.

2.4 Plasma monitoring

The light emitted from plasma was transmitted through a linear bundle of 10 channel optical fibers, which simultaneously record the optical emission from a 40 mm length strip (parallel to the plasma expansion axis). Optical spectra were collected by an iHR550 Imaging Spectrometer (Horiba) using 1200/mm. Plasma image was recorded with a LN_2 cooled Symphony CCD camera having 2048 × 512 pixels (Horiba) in a wavelength range of 200 – 900 nm. During the deposition process, the optical emission of the plasma was recorded using a 10-linear bundle full-range optical fiber connected to high resolution spectrometer. An optical arrangement of two lenses was used to define 0.3 mm of plasma. The fiber was positioned at various distances with respect to the target (1–30 mm) to extract the spatial distribution of the species within the plasma volume.

3 Results and discussions

3.1 In situ plasma monitoring

In Fig. 2, we have plotted a representative spectrum recorded at 1 mm from the target for depositions performed at 5 Pa of O_2 pressure and the pressure effect on the individual species emission. Using a specialized database emission lines for atomic species of Lu (411 nm), Mo (605 nm), Eu (513 nm) and corresponding ionic species and O (Lu II – 621 nm; Eu II – 363 nm and O II – 383 nm), were identified [34]. With the increase of the background pressure from 10^{-4} Pa to 5 Pa we observe an all-round increase of approximately 50% in line intensity Mo, Eu with only a slight increase in O ionic lines and a decrease in the intensity of Lu atoms. In Fig. 2(a) we observe two interesting features at 465 nm and 516 nm. These two signatures are identified as molecular emission from LuO molecule. At 465 nm the emission it corresponds to the $C^2\Sigma^+$ molecular state while at 516 nm it corresponds to the emission from the A ($^2\Pi_{1/2}$) state [24, 34].

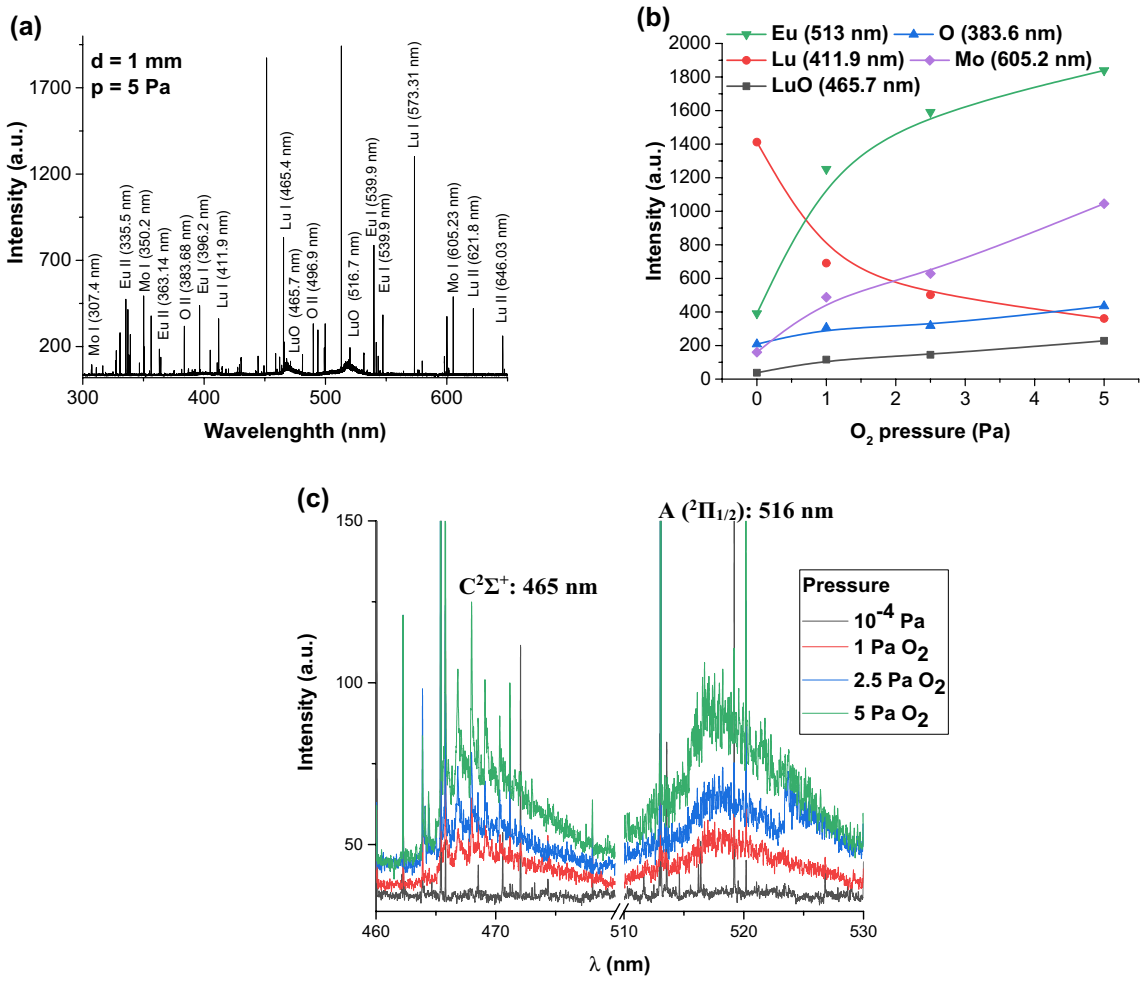

Fig. 2 Discrete emission of a Lu_2O_3: Mo, Eu 5% laser ablation plasma (**a**) recorded at 1 mm from the target (10 µs gate width),the pressure impact on the line emission intensity for composing species, lines in the graphs are a guide to the eye (**b**) and comparative representation of LuO molecular emission for each investigated pressure (**c**)

At low pressures, the molecular signatures for LuO cannot be seen indicating a complete breakdown of the target lattice. With the addition of O_2 the intensity of both $C^2\Sigma^+$ and A ($^2\Pi_{1/2}$) LuO emission increases. The decrease of the Lu atoms intensity is directly correlated with the increase in molecular emission of LuO: $C^2\Sigma^+$ state. By increasing the O_2 pressure, we enhance the reactions between Lu-O through collisions leading to a recombination process at the edge of the plume. The re-formation of the LuO molecule at the edge of the plasma is a well-known mechanism and it is based on the thermodynamical optimum conditions for the chemical reaction to occur. This result is also supported by the decrease in mean free math of about 3 orders of magnitude with the variation of the background pressure from 10^{-4} Pa to 5 Pa and an increase in collision frequency with a factor of 16.

The formation of complex molecules in laser produced plasma can reportedly, have two origins. A certain amount of molecular density can be ablated directly from the target by means of thermal mechanism as it was shown in [35] for MgO molecules or by the lattice breaking after the Coulomb explosion mechanisms, as it is the case for graphite in certain laser fluence ranges [36]. Higher fluences with respect to the ablation threshold can induce a complete breakdown of the lattice structure and the molecular bonds. This aspect can be seen in Fig. 2c where no molecular signatures were recorded in high vacuum conditions. In Fig. 3a the space resolved measurements reinforces these results as LuO emission is not seen at all throughout the plasma volume. For the investigated samples at a 4.6 eV per each photon interacting with the lattice at a fluence of 5 J/cm^2 we are above the reported ablation threshold of 1.5 J/cm^2. These particular irradiation conditions mean that per pulse a photon flux of $8 \cdot 10^{11}$ W/cm^2 will hit the target leading to molecule bonding breaking as LuO requires only 7 eV and Eu–O 5 eV. The electrostatic ablation mechanism is here secondary as

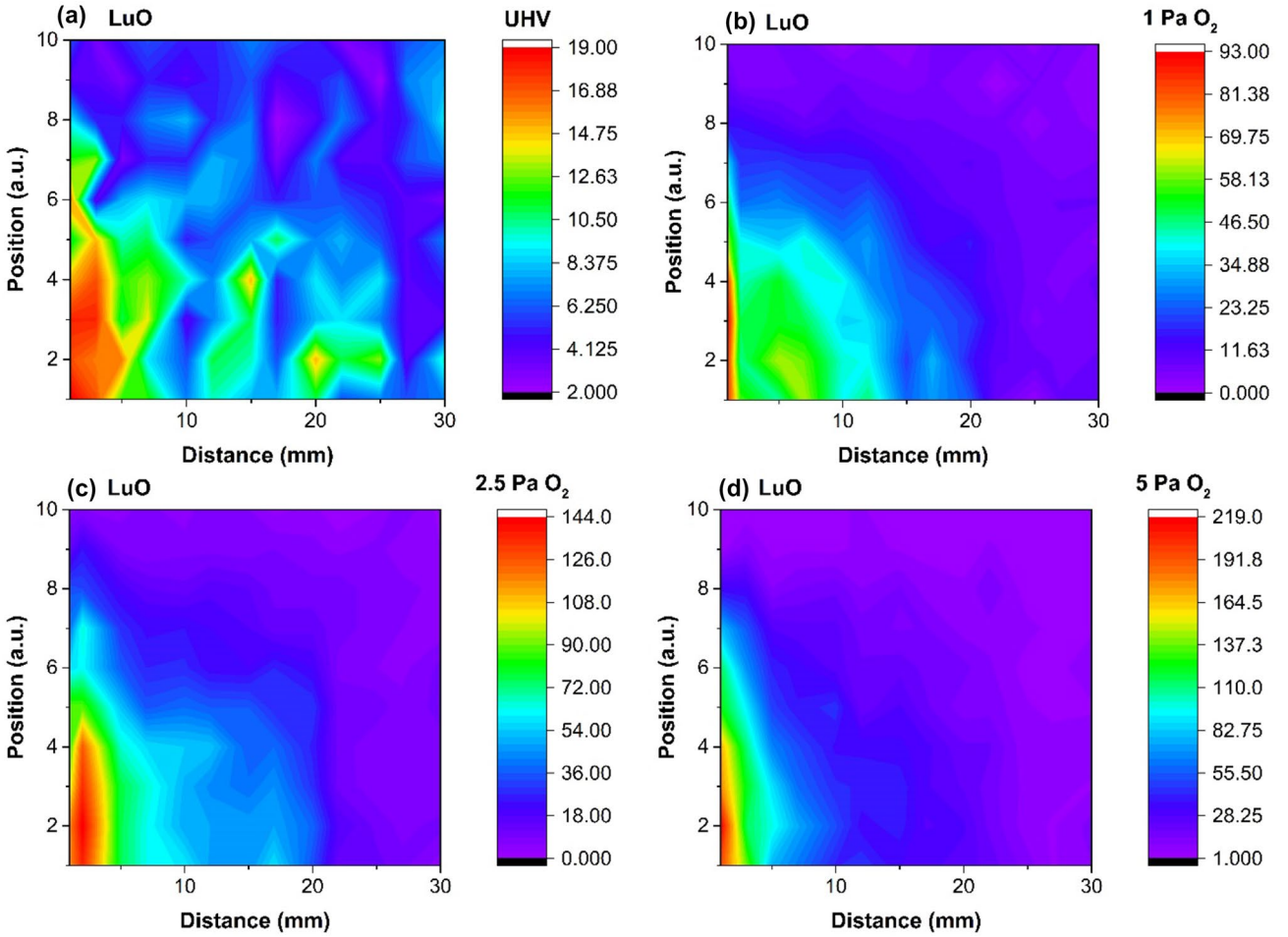

Fig. 3 Spatial distribution of LuO (456 nm) emission intensity for 10^{-4} Pa (**a**), 1 Pa O_2 (**b**), 2.5 Pa O_2 (**c**) and 5 Pa O_2 (**d**) from plasma generated on Lu_2O_3: Mo, Eu 5%

the photon energy is below the Lu_2O_3 band gap of 5.5 eV, therefore, the main ablation mechanisms will be of thermal nature (melting, explosive boiling, evaporation, etc.). Extreme cases of melting and explosive boiling process can lead to the formation and the expulsion of clusters. However, the addition of Mo is aimed towards inhibiting the extreme thermal ablation process and reduce the quantity of ejected clusters. Mo has higher melting and boiling temperatures 1.5 times higher than the respective values of Lu and 2.6 times higher than characteristic temperatures of Eu, therefore will act as an inhibitor for the kinetic explosion of material from the target. Both oxide bonds (MoO and LuO) existent in the target have similar dissociation energy 5.2 eV for MoO and 6.86 for LuO which means that the laser beam energy will be equally used to eject Mo, and Lu from the target reducing the change for cluster formation. The LuO molecule can reform throughout the plasma volume as we can see in Fig. 3b–d where we have presented the mapping of the $C^2\Sigma^+$ LuO spectral region intensity for relatively high O_2 pressures. For 1 Pa and 2.5 Pa the emission stretches out until 2.5 cm while at 5 Pa the emission is enhanced and limited to 1 cm spatial expansion. Due to the proportional increase in LuO emission with the increase of the O_2 pressure, we can conclude that the main molecular density comes from recombination with the background gas. The spatial distribution of LuO (Fig. 3b-d) reveals a non-monotonic decrease of molecular emission from the target towards the substrate. Several peaks in LuO emission are seen and might reveal complex self-organization of the LPP during the deposition process.

To further investigate the self-structuring scenario suggested by the previous results, we have represented the distribution of O, Lu, Mo, and Eu atoms (Fig. 4). The spatial distribution reveals the presence of multiple maxima for all investigated species. This implies that the structuring of the plasma is a general attribute of the whole plasma plume and it is not induced by individual particle segregation as it was reported by Schou's group [14] where they showcase that within the spatial distribution of element lighter elements have higher velocities and they are placed towards the edge of the plume while the heavier

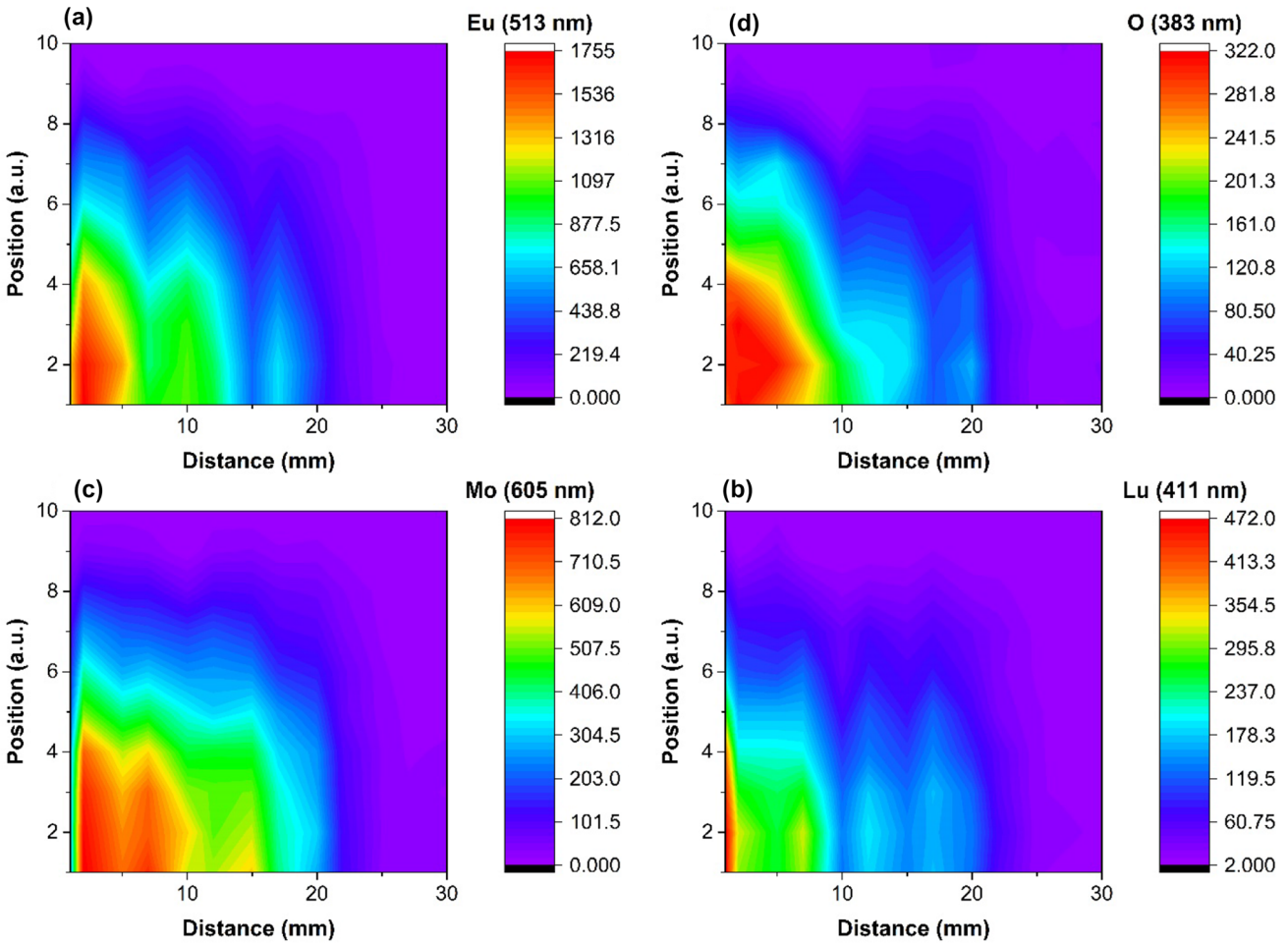

Fig. 4 Spatial distribution of Eu (**a**), Lu (**b**), O (**c**) and Mo (**d**) species at 1 Pa of O_2 in a Lu_2O_3:Mo, Eu 5% plasma

are forming the core result also confirmed by theoretical modeling of multi-element metallic alloy LPP [37]. Differential particle evaporation or acceleration in the transient double layer formed at the front of the plume are often suggested in the literature as the main driving mechanism in multi-element – multi-structured plasmas. Implementing the same principles for LuO:Eu, Mo plasma and considering the particularities of our data, one can estimate an average expansion velocity (over 10 μs) for each recorded maxima emission. For all the investigated elements we can distinguish three maxima that can be attributed to three plasma structure expanding with different velocities (1st – 2 km/s, 2nd – 0.7 km/s and 3rd – 0.1 km/s). The values determined for the expansion velocities are relatively lower than those reported for other configurations. Lower velocities can reflect a higher threshold value induced by the Mo addition and also, they need to be understood as average values over the integration time. The symmetry in the spatial distribution for all species is also seen as a signature for a stoichiometric composition of the ablated cloud during the PLD process and subsequent stoichiometric transfer on the thin films.

Further analysis over the laser-plasma plume's inner energy requires the implementation of spectral analysis methods like Boltzmann Plot [38] and Stark widening [39] techniques. For the determination of electron excitation temperature, Boltzmann plot method was implemented by plotting the data from all the observed emission lines, which will offer a global dimension of the resulted values. The values obtained for the LuO roto-vibrational temperature, calculated for $C^2\Sigma^+$ signature and the electron excitation temperature are presented in Fig. 5(a). We report here on a steady increase in molecular temperature, reaching a maximum of 1 eV at 5 Pa while the excitation temperature increases with the initial addition of O_2 reaching a maximum of 2.6 eV at 1 Pa followed by a decrease. We can identify two regions: below 2.5 Pa the atomic interactions are dominant with low molecular emission and a maximum excitation temperature and density and a second one above 2.5 Pa where the molecular energy is maximum and the electron excitation

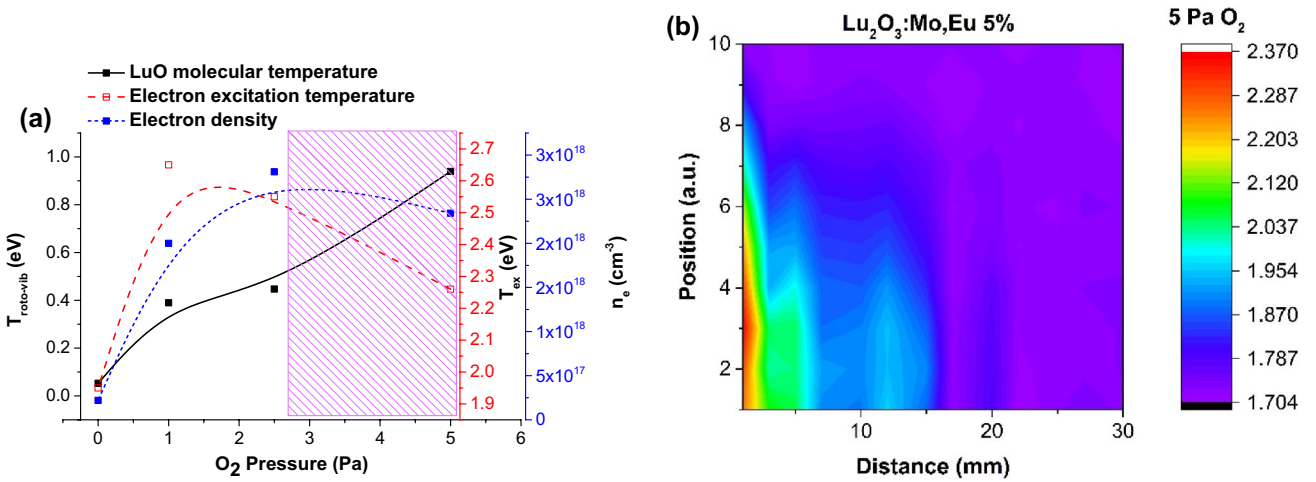

Fig. 5 O_2 pressure effect on electron excitation temperature, electron density and LuO molecular temperature, lines in the graphs are a guide to the eye (**a**) and spatial distribution of electron excitation temperature for Lu_2O_3:Mo, Eu 5% in 5 Pa of O_2 (**b**)

temperature slightly decreases. The simultaneous increase of the background gas leads to the decrease of the mean free path of about 4 orders of magnitude and subsequently the increase in the number of collision and neutralization of ions and plasma thermalization. A strong increase in the thermal plasma energy coupled with a proximity to the local thermodynamical equilibrium (from a Boltzmann plot and McWhirter perspectives) increases the probability of a stoichiometric deposition process [1].

3.2 Thin film analysis

For thin film deposition of Lu_2O_3:Eu at low substrate temperature an amorphous structure is expected, according to reports from literature[40]. In Fig. 6a, we have represented the diffraction patterns for various growth conditions. In our case all films have two wide peaks at $2\theta = 31.2°$ and $2\theta = 53.5°$, which correspond to amorphous phase of Lu_2O_3 films. The O_2 pressure significantly influence on the crystallinity of the films. Thus, the degree of crystallinity decreases with increasing oxygen pressure. The films are amorphous-polycrystalline and have only one cubic crystalline phase (space group I 21 3) with a lattice parameter $a = (1.039 \pm 0.002)$ nm. The wide peak at $2\theta = 21°$ is a reflection from the fused silica substrate. Due to shielding effect induced by the deposited films we see a decrease in the peak intensity with the increase in film thickness. With the increase in the O_2 pressure we observe a decrease in crystallite size and transitions towards complete amorphous structures. This evolution is due to the decrease in particle energy and a clearer presence of molecular species in plasma which will inhibit the kinetic energy of the atomic species thus reducing their arrival energy on the surface limiting their movement. When analyzing he morphology of the

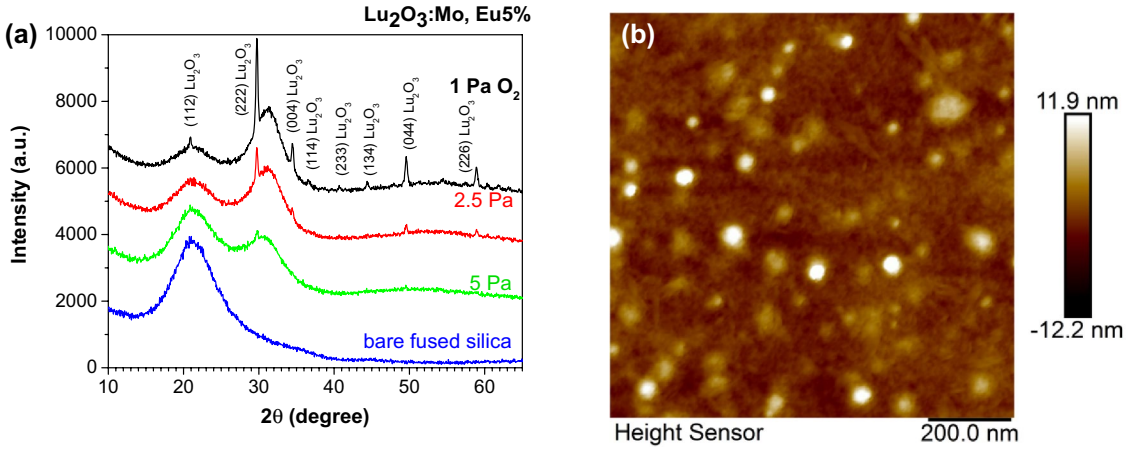

Fig. 6 Diffraction patterns for various growth conditions (**a**) and a selective AFM image for the 1 Pa O_2 deposition conditions (**b**)

film, we observe that all the deposited films were amorphous with embedded nanoparticles. A representative AFM image of Lu_2O_3:Mo, Eu 5% film deposited at room temperature in 1 Pa of O_2 is presented in Fig. 6(b). We note the presence of nanoparticles having on average 40 nm in diameter embedded in the amorphous matrix. Since the XRD data revealed diffraction peaks characterizing the cubic phase of the Lu_2O_3:Eu it results that the peaks are given by the polycrystalline nanoparticles immersed in the amorphous matrix.

To further investigate the quality of the deposited films we performed fluorescence spectroscopy measurements. The emission spectra were excited at $\lambda = 254$ nm via the charge transfer band from interaction between $O^{2-} \rightarrow Eu^{3+}$ [41–43]. In Fig. 7 we presented the Eu^{3+} emission spectra for the $^5D_0 \rightarrow {}^7F_{0,1,2}$ transition range for different deposition conditions. The magnetic dipole $^5D_0 \rightarrow {}^7F_1$ transition is originating from Eu^{3+} in the C_2 (noncentrosymmetric) and S_6 (centrosymmetric) sites, while hypersensitive electric dipole transition $^5D_0 \rightarrow {}^7F_1$ is arising from Eu^{3+} exclusively in the C_2 site [42, 44].We can observe the most intense peak at 611 nm characteristic for the cubic phase [44] attributed to the $^5D_0 \rightarrow {}^7F_2$ transition. With the increase of the O_2 pressure we notice an increase in the overall intensity and with more peaks becoming dominant in the 605 – 640 nm range. To highlight each contribution to the photoluminescence (PL) spectra we performed a deconvolution of the 605 – 635 nm range (Fig. 7b). We observed supplementary emission peaks at 615 nm and 625 nm which could be attributed as the contribution of Eu^{3+} located in the B and C site of the monoclinic phase as was presented in [40]. However, in our present work, we do not find any evidence from monoclinic phase by means of XRD analyses. Due to this fact, the shoulder at 615 nm and broad line at 625 nm are a consequence of the luminescence of Eu^{3+} ion located on the surface of the nanocrystals, which occupy the positions with lower symmetry compare to the ions located in the center of cubic Lu2O3 nanocrystals as was demonstrated for similar Eu:Y_2O_3[40]. Based on the results of optical emission spectroscopy we can conclude that the transition from nanocrystalline films to a complete amorphous thin film is aided by a high electron density regime with enhanced molecular contributions and a lower electron temperature. For the generation of cubic structure nanoparticle, the plasma regime is dominated by atomic emission with high electron temperatures and reduced contribution from the molecular species.

4 Conclusion

The PLD process of Lu_2O_3:Mo, Eu (1%, 3%, 5%) was investigated by in-situ optical emission spectroscopy. The investigations revealed the formation of a quasi-stoichiometric cloud of particles containing elements from the irradiated target. The spatial distribution of individual elements revealed the plasma structuring in three substructures traveling with different expansion velocities. The kinetic and the thermal energy of the plasma were controlled by the Mo doping of the target by increasing the ablation threshold and by adding O_2 as a working gas. The role of O_2 was twofold: for the reformation of the Lu_2O_3 structure at the substrate and to thermalize the plasma.

The formation of LuO molecule within the plasma plume was seen through the spectral signatures of $C^2\Sigma^+$ and A ($^2\Pi_{1/2}$) with the addition of a minim1 Pa of O_2, when the O_2 medium becomes favorable for molecular structure formation during plasma expansion. The energy of the ejected particles was controlled through doping and O_2 pressure. The effect of O_2 pressure over the plasma energy revealed a transition from an atomic dominated region towards a molecular dominated one. The deposited films contain nanocrystalline films with an amorphous matrix. The decrease in plasma energy reduces the volume of nanocrystalline and results in

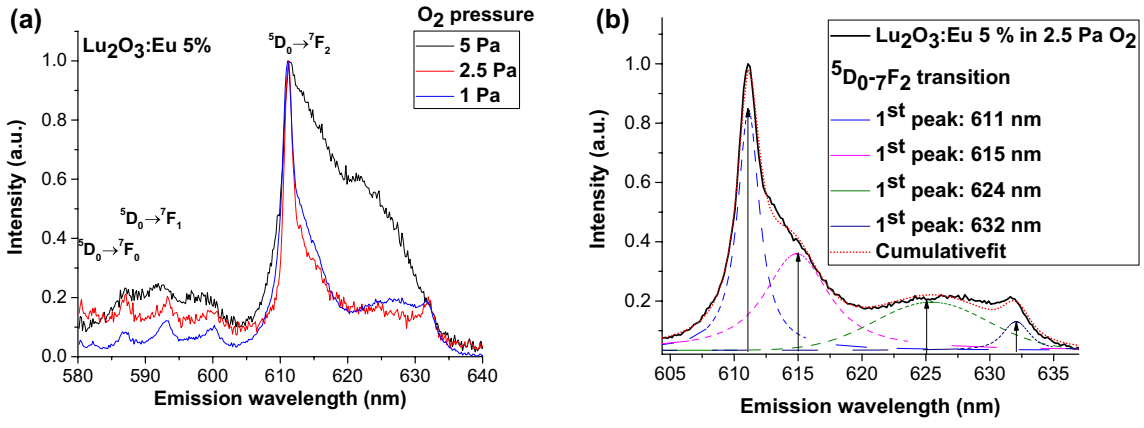

Fig. 7 $^5D_0 \rightarrow {}^7F_{0,1,2}$ emission spectra for Lu2O3:Eu 5% films generated for different O_2 pressures (**a**) and a peak deconvolution highlight for Lu2O3:Mo, Eu 5% in 2.5 Pa of O_2 (**b**)

amorphous films. The low level codoping with Mo does not affect the outcome of the deposition with little to no changes to the thin film in terms of structure or the luminescence properties of the thin film. The change in the dynamical regime of the plasma directly affects the morphology of the films with the addition of O_2 the films becoming predominantly amorphous.

Supplementary Information The online version contains supplementary material available at https://doi.org/10.1007/s00340-021-07689-4.

Acknowledgements This work was supported by Czech Science Foundation, project 18-17834S, by Romanian Ministry of Education and Research, under Romanian National Nucleu Program LAPLAS VI – contract n.16N/2019, ELI-RO_2020_12 and Postdoctoral Project PD 145/2020. We acknowledge the Operational Program Research, Development and Education financed by European Structural and Investment Funds and the Czech Ministry of Education, Youth and Sports SOLID21 CZ.02.1.01/0.0/0.0/16_019/0000760.

Author contributions Conceptualization: SI, MN; methodology: SI, MN, JM-C, JL; formal analysis and investigation: JM-C, SC, LF, ŠH, MP, TZ, KK; writing – original draft preparation: SI, MN, JM-C, JL; writing – review and editing: SC, KK, JL, MN; Resources: JL, MN; supervision: JL, MN.

References

1. J. Schou, Appl. Surf. Sci. **255**, 5191–5198 (2009)
2. A.A. Puretzky, D.B. Geohegan, R.E. Haufler, R.L. Hettich, X.Y. Zheng, R.N. Compton, AIP Conf. Proc. **288**, 365–374 (1993)
3. S. Irimiciuc, R. Boidin, G. Bulai, S. Gurlui, P. Nemec, V. Nazabal, C. Focsa, Appl. Surf. Sci. **418**, 594–600 (2017)
4. M. Skočić, D. Dojić, S. Bukvić, J. Quant. Spectrosc. Radiat. Transf. **227**, 57–62 (2019)
5. S.A. Irimiciuc, S. Chertopalov, V. Craciun, M. Novotný, J. Lancok, Plasma Process. Polym. **1**, 1–9 (2020)
6. C. Aragón, J.A. Aguilera, Spectrochim. acta Part B At. Spectrosc. **63**, 893–916 (2008)
7. S.A. Irimiciuc, B.C. Hodoroaba, G. Bulai, S. Gurlui, V. Craciun, Spectrochim. Acta - Part B At. Spectrosc. **165**, 105774 (2020)
8. S.S. Harilal, C.V. Bindhu, M.S. Tillack, F. Najmabadi, A.C. Gaeris, Appl. Phys. **93**, 2380–2388 (2003)
9. S.S. Harilal, C.V. Bindhu, M.S. Tillack, F. Najmabadi, A.C. Gaeris, J. Phys. D. Appl. Phys. **35**, 2935–2938 (2002)
10. S. Canulescu, E.L. Papadopoulou, D. Anglos, T. Lippert, C.W. Schneider, A. Wokaun, J Appl. Phys. **105**, 063107 (2009)
11. S.A. Irimiciuc, P.E. Nica, M. Agop, C. Focsa, Appl. Surf. Sci. **506**, 144926 (2020)
12. D.B. Geohegan, A.A. Puretzky, Appl. Surf. Sci. **96–98**, 131–138 (1996)
13. A. Ojeda-G-P, C.W. Schneider, M. Döbeli, T. Lippert, A. Wokaun, J. Appl. Phys. **121**, 135306 (2017)
14. M. Bator, Y. Hu, M. Esposito, C.W. Schneider, T. Lippert, A. Wokaun, Appl. Surf. Sci. **258**, 9355–9358 (2012)
15. A.A. Puretzky, D.B. Geohegan, X. Fan, S.J. Pennycook, Appl. Phys. A Mater. Sci. Proc. **70**, 153–160 (2000)
16. P. Darmawan, P.S. Chia, P.S. Lee, J. Phys. Conf. Ser. **61**, 046 (2007)
17. J.M.J. Lopes, M. Roeckerath, T. Heeg, E. Rije, J. Schubert, S. Mantl, V.V. Afanas, S. Shamuilia, A. Stesmans, Y. Jia, D.G. Schlom, Appl. Phys. Lett. **89**, 311–318 (2006)
18. P. Mandal, U.P. Singh, S. Roy, IOP Conf. Ser. Mater. Sci. Eng. **872**, 012062 (2020)
19. D. Sengupta, S. Miller, Z. Marton, F. Chin, V. Nagarkar, G. Pratx, Adv. Healthc. Mater. **4**, 2064–2070 (2015)
20. X.J. Liu, H.L. Li, R.J. Xie, N. Hirosaki, X. Xu, L.P. Huang, J. Lumin. **127**, 469–473 (2007)
21. J. Wang, Q. Liu, Q. Liu, J. Mater. Chem. **15**, 4141–4146 (2005)
22. S. Bär, G. Huber, J. Gonzalo, A. Perea, A. Climent, F. Paszti, Mater. Sci. Eng. B Solid-State Mater. Adv. Technol. **105**, 30–33 (2003)
23. K. Kaminaga, D. Oka, T. Hasegawa, T. Fukumura, ACS Omega **3**(10), 12501–12504 (2018)
24. S.A. Cooke, C. Krumrey, M.C.L. Gerry, J. Mol. Spectrosc. **267**, 108–111 (2011)
25. A.K. Pradhan, K. Zhang, S. Mohanty, J. Dadson, D. Hunter, B. Loutts, J. Appl. Phys. **97**, 023513 (2005)
26. V. Petrícek, M. Dušek, L. Palatinus, Zeitschrift Fur Krist. **229**, 345–352 (2014)
27. R.W. Cheary, A.A. Coelho, J.P. Cline, J. Res. Natl. Inst. Stand. Technol. **109**(1), 1 (2004)
28. A. Pavlik, S.V. Ushakov, A. Navrotsky, C.J. Benmore, R.J.K. Weber, J. Nucl. Mater. **495**, 385–391 (2017)
29. A. Belkly, M. Helderman, V.L. Karen, P. Ulkch, Acta Crystallogr. Sect. B Struct. Sci. **58**, 364–369 (2002)
30. M.V. Abrashev, N.D. Todorov, J. Geshev, J. Appl. Phys. **116**, 103508 (2014)
31. W.B. White, V.G. Keramidas, Spectrochim. Acta **28**, 501–509 (1972)
32. M. Dieterle, G. Mestl, Phys. Chem. Chem. Phys. **4**, 822–826 (2002)
33. D.R. Lide, *Handbook of Chemistry and Physics, National Institute of Standards and Technology* (CRC Press, 2005)
34. A. Kramida, Y. Ralchenko, J. Reader, NIST ASD Team, NIST atomic spectra database lines form, NIST At. Spectra Database (Ver. 5.2) [Online]. 2014.
35. P. Płóciennik, D. Guichaoua, A. Zawadzka, A. Korcala, J. Strzelecki, P. Trzaska, B. Sahraoui, Opt. Quant. Electron. **48**, 277 (2016)
36. N.M. Bulgakova, R. Stoian, A. Rosenfeld, I.V. Hertel, E.E.B. Campbell, Phys. Rev. B. **69**, 054102 (2004)
37. S.A. Irimiciuc, S. Gurlui, M. Agop, Appl. Phys. B. **125**, 1–11 (2019)
38. T. Belmonte, C. Noël, T. Gries, J. Martin, G. Henrion, Plasma Sources Sci. Technol. **24**, 064003 (2015)
39. D.W. Hahn, N. Omenetto, Appl. Spectrosc. **64**, 335–366 (2010)
40. C. Martinet, A. Pillonnet, J. Lancok, C. Garapon, J. Lumin. **126**, 807–816 (2007)
41. Q.I. Yang, J. Zhao, L. Zhang, M. Dolev, A.D. Fried, A.F. Marshall, S.H. Risbud, A. Kapitulnik, Appl. Phys. Lett. **104**(8), 082402 (2014)
42. C.C.S. Pedroso, J.M. Carvalho, L.C.V. Rodrigues, J. Hölsä, H.F. Brito, ACS Appl. Mater. Interf. **8**, 19593–19604 (2016)
43. K. Binnemans, Coord. Chem. Rev. **295**, 1–45 (2015)
44. M. Xu, W. Zhang, N. Dong, Y. Jiang, Y. Tao, M. Yin, J. Solid State Chem. **178**, 477–482 (2005)